112

AN INVESTIGATION OF AEROELASTIC ROTORCRAFT-PILOT INTERACTION

Pierangelo Masarati, Giuseppe Quaranta

Dipartimento di Ingegneria Aerospaziale, Politecnico di Milano
{masarati,quaranta}@aero.polimi.it

Massimo Gennaretti, Jacopo Serafini

Dipartimento di Ingegneria Meccanica e Industriale, Università Roma Tre
{m.gennaretti,serafini}@uniroma3.it

Abstract

This paper presents the analysis of aeroelastic Rotorcraft-Pilot Coupling (RPC) problems. The structural dynamics of the airframe and of the rotor, and the dynamics of the control system, including the passive biomechanics of the pilot, are modeled using a free general-purpose multibody solver. The aerodynamics of the main rotor is modeled using an original free wake implementation based on the Boundary Element Method (BEM). The analysis is applied to the collective bounce problem, by assessing the existence of the phenomenon and the appropriateness of the aerodynamic and aeroservoelastic model for its analysis. The influence of various properties of the model on the stability of the response is discussed as well.

1 INTRODUCTION

This paper illustrates a joint activity between research groups of the Universities Roma Tre and Politecnico di Milano for the investigation of aeroelastic Rotorcraft-Pilot Coupling (RPC). The interaction of helicopter dynamics and aeroservoelasticity with the pilot in a frequency band characteristic of rotorcraft aeroelasticity is analyzed. The presence of the pilot in the control loop may cause the unintentional transmission of the vibratory motion of the rotorcraft through the control inceptors.

Unintentional commands can degrade performances and handling qualities. McRuer noted that in some cases the pilot can destabilize the system [1]. As a consequence of a trigger event, pilots can introduce voluntary although unintentionally incorrect commands because of an incorrect perception of the aircraft behavior, resulting in Pilot-Induced Oscillations (PIO). When the unintended commands are introduced by an involuntary intervention, often because related to higher frequency dynamics, the result is often indicated as Pilot-Assisted Oscillations (PAO).

These problems received significant attention in fixed wing aircraft in the last decades, since the introduction of significant control augmentation. Rotorcraft analysis received less attention than fixed wing with respect to PAO. The passive biomechanics of rotorcraft pilots, with respect to the collective control, has been studied by Mayo in 1989 [2]. Bell Helicopter took pilot biomechanics into account during the development of the V-22 [3], and incorporated it in the design of the BA-609 [4]. Reports of Rotorcraft-Pilot Coupling (RPC) with US Navy helicopter operation have been presented by Walden [5].

During an exploratory activity performed by GARTEUR HC AG-16, key aspects of RPC have been discussed and highlighted. A classification of RPC has been proposed, based on the frequency of oscillatory phenomena that characterize the problem [6]. PIOs are usually related to flight dynamics, in the range up to 1 Hz, while PAOs typically occur at frequencies between 2 Hz and 8 Hz, and are associated with aeroelastic phenomena. The distinction is relatively straightforward for fixed-wing aircraft. However, rotary-wing aircraft may show significant overlapping since a broad band of frequencies impacts flight dynamics while being close to pilot limbs' intrinsic biodynamics. This paper summarizes the numerical simulation activity performed by Roma Tre and Politecnico di Milano, originating from the GARTEUR activity, continued within a national project in partnership with other Italian universities, and now further pursued within the EC 7th Framework Programme ARISTOTEL (http:

//www.aristotel.progressima.eu/), to investigate the key aspects of the phenomenon.

2 MODELING AND ANALYSIS APPROACH

Specific rotorcraft aeromechanics aspects characterize their interaction with the pilot's passive biomechanics. Aeroservoelastic models based on Multibody System Dynamics (MSD) and Boundary Element Method (BEM) aerodynamics of rotorcraft are used to describe essential aspects of the problem including: main and tail rotor aeromechanics and aeroelasticity, airframe dynamics, control systems servodynamics.

The passive biomechanics of the pilot is modeled for specific controls using transfer functions available from the literature [2, 3]. Analogous transfer functions subsequently identified from results obtained in dedicated test campaigns performed in cooperation with the University of Liverpool using the 'Bibby' flight simulation facility [7] are considered as well. Their application to the aeroservoelastic analysis of rotorcraft [8] allowed to investigate the influence of unsteady aerodynamics and airframe dynamics modeling on RPC proneness [8, 9, 10].

A critical aspect consists in determining the most appropriate aeroelastic modeling detail that allows to efficiently capture the essence of the phenomenon. The availability of suitable pilot models is also essential, since the pilot's passive impedance represents the uncertain phase shift and gain that may alter the stability of the system by feeding the rotorcraft vibration back into the control chain.

As discussed in previous works [8], the appearance of adverse couplings is related to simultaneously considering: a) pilot's feedthrough, b) rigid-body motion of the rotorcraft, c) deformability of the blades and d) of the airframe, all coupled by the rotor aerodynamics.

These aspects are duly taken into account in the analysis by merging the structural dynamics and multidisciplinary capabilities of the MSD solver with the accurate yet efficient modeling of aerodynamic loads provided by the BEM solver [11, 10]. The influence of free wake modeling on hover and forward flight stability has been addressed in [12]. Aspects related to tiltrotor aeroelasticity in interaction with the pilot's passive biodynamics have been considered as well [13, 14, 15]. The capabilities of the proposed coupled solver are used to investigate the problem in detail.

2.1 Structural Dynamics

The structural dynamics of the helicopter are modeled using the free general-purpose multibody solver MBDyn (http://www.mbdyn.org/), developed by the Aeroservoelasticity and Structural Dynamics research group of the 'Dipartimento di Ingegneria Aerospaziale', Politecnico di Milano. The approach is quite general: the MSD solver can directly address many aspects of the problem, including aeroelasticity itself, although built-in aerodynamics is limited to Blade Element/Momentum Theory (BE/MT), while provisions exist to delegate fluid dynamics to external solvers [16, 17, 18]. However, an efficient and accurate rotor aerodynamics solver, capable of dealing with massive aeroservoelastic analyses required by RPC, is not available internally. As a consequence, in this work aerodynamics is delegated to an external solver, discussed in the next section.

The structural model consists of the main rotor and the airframe. The rotor, sketched in Fig. 1, is modeled using the multibody approach: kinematically exact constraints, enforced by means of Lagrange multipliers, describe the relative motion between the rigid bodies that constitute the hub, the blade bearings and the pitch control mechanism, while structural dynamics is dealt with by nonlinear Finite Element (FE) beam elements based on an original Finite Volume (FV) formulation [19], and by lumped masses.

The airframe is modeled using the Component Mode Synthesis (CMS) approach. The CMS model accounts for the arbitrary rigid-body motion of the airframe, with superimposed structural deformation modeled by selected Normal Vibration Mode (NVM) shapes, whose frequency is within the range of interest, and with a non-negligible participation of the motion of the rotor attachment and crew seat points. The NVM have been computed with the rotor mass lumped at the connection point. The rotor mass has been subsequently removed from the modal mass matrix, according to the fictitious masses approach [20], since the rotor mass is already contributed by the multibody model of the rotor. The interface between the CMS model and the MSD domain occurs at selected points, including the main rotor attachment, the tail rotor attachment (although the tail rotor is approximated by a lumped force) and the seats of the pilot and of the co-pilot. The main rotor is connected to the airframe by a revolute joint that enforces the relative angular velocity.

Although a complete model of the free-flying he-

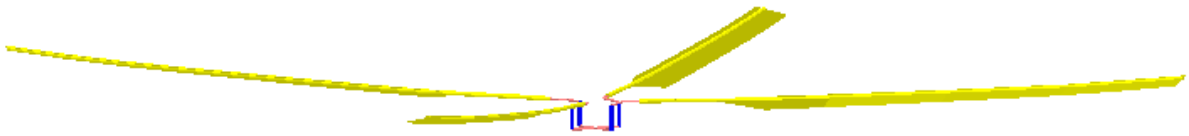

Figure 1: Sketch of the main rotor structural dynamics model.

licopter, including the tail rotor, has been developed, for the purpose of this investigation the overall rigid-body motion of the helicopter is selectively constrained to enforce the desired flight condition. Only the rigid-body degrees of freedom deemed important for each specific analysis are allowed.

2.2 Aerodynamics

The aerodynamics that govern the forces acting on a helicopter are dominated by the unsteady behavior of the main rotor and its inflow on the fuselage, the tail rotor and the other aerodynamic surfaces. The accurate analysis of problems involving the interaction between vortexes and bodies requires the application of specifically designed three-dimensional, unsteady aerodynamic solvers. The boundary integral formulation for potential flows introduced in [21], developed by the Aeroelasticity research group of the 'Dipartimento di Ingegneria Meccanica e Industriale', Università Roma Tre, is used in this work.

It represents an enhancement of the formulation proposed in 1974 by Morino [22], which overcomes numerical solution instabilities caused by the impingement of the wake on body surfaces. This formulation introduces the decomposition of the potential field into an incident, φ_I, and a scattered potential field, φ_S. The scattered potential is generated by sources and doublets over the body surfaces, and by doublets over portions of the body wakes very close to the trailing edges they emanated from (near wake, S_W^N). The incident potential is generated by doublets over the complementary wake regions that compose the far wakes, S_W^F. These wake portions may impinge on other surfaces.

The scattered potential is discontinuous across S_W^N, whereas the incident potential is discontinuous across S_W^F. Hence, as demonstrated in [21], for $\varphi = \varphi_I + \varphi_S$ the scattered potential is obtained by

$$\varphi_S(\mathbf{x},t) = \int_{S_B} \left[G(\chi - \chi_I) - \varphi_S \frac{\partial G}{\partial n} \right] \mathrm{d}S(\mathbf{y}) - \int_{S_W^N} \Delta\varphi_S \frac{\partial G}{\partial n} \mathrm{d}S(\mathbf{y}), \quad (1)$$

where G is the unit source solution and $\Delta\varphi_S$ is the potential jump across the wake surface [21]. In addition, $\chi = \mathbf{v}\cdot\mathbf{n}$ accounts for the impenetrability boundary condition ($\mathbf{v}$ denotes the body velocity due to rigid and elastic body motion; $\mathbf{n}$ is the surface unit outward normal vector), while $\chi_I = \mathbf{u}_I \cdot \mathbf{n}$, with the velocity induced by the far wake, $\mathbf{u}_I = \nabla\varphi_I$, given by

$$\mathbf{u}_I(\mathbf{x},t) = -\nabla \int_{S_W^F} \Delta\varphi_S \frac{\partial G}{\partial n} \mathrm{d}S(\mathbf{y}). \quad (2)$$

The incident potential affects the scattered potential by the induced-velocity term, χ_I; in turn, the scattered potential affects the incident potential by its trailing-edge discontinuity that is convected along the wake and yields the intensity of the doublet distribution over the far wake.

Equation (2) is discretized with a zero-order discretization using N panels over the far wakes. Recalling the vortex-doublet equivalence, the incident velocity field may be evaluated using

$$\mathbf{u}_I(\mathbf{x},t) \approx -\sum_{n=1}^{N} \Delta\varphi_S\left(\mathbf{y}_{W_n}^{TE}, t-\theta_n\right) \int_{C_n} \nabla_{\mathbf{x}} G \times \mathrm{d}\mathbf{y}, \quad (3)$$

where C_n denotes the contour line of the n-th far wake panel, $\mathbf{y}_{W_n}^{TE}$ is the trailing edge position where the wake material point currently in $\mathbf{y}_{W_n}$ emanated at time $t-\theta_n$, and $\nabla_{\mathbf{x}}$ denotes the gradient with respect to $\mathbf{x}$. This equation represents the velocity field given by the Biot-Savart law applied to the vortexes having the shape of the far wake panel contours and intensity $\Delta\varphi_S(\mathbf{y}_{W_n}^{TE}, t-\theta_n)$.

A finite-thickness core is introduced in those vortexes where a regular distribution of the induced velocity is guaranteed, along with a stable and regular solution even in body-vortex impact conditions [21] (this may only affect the far wake).

Once the potential field is known, the Bernoulli theorem yields the pressure distribution and the corresponding aerodynamic loads are obtained by integration over the surface of the bodies.

The aerodynamic solution may be obtained considering either a prescribed wake shape or a wake shape distorted in accordance with the resulting velocity field (free-wake analysis). The free-wake shape is obtained starting from the numerical evaluation of the potential gradient (remember that in this aerodynamic formulation $\mathbf{u} = \nabla\varphi$) at the wake material points that represents their velocity in a frame of reference fixed with the undisturbed air. Thus, for $\Delta\mathbf{x}_w(t)$ denoting the distance between the position of a wake material point at the current time t and the position of the same wake material point at the instant when it was emitted by the trailing edge, the following equation may be written

$$\frac{\mathrm{d}}{\mathrm{d}t}\Delta\mathbf{x}_w = \mathbf{u}. \tag{4}$$

Equation (4) is integrated through the Crank-Nicolson method and the wake shape is renewed accordingly. Note that the numerical scheme leaves the time integration step uncorrelated with respect to the azimuthal spatial discretization of the wake, thus allowing a finer wake mesh close to the trailing edge (thus accelerating numerical convergence) combined with an efficient aeroelastic coupling with the structural dynamics equations.

Figure 2 shows a free-wake shape obtained for a two-blade helicopter rotor in forward flight at an advance ratio $\mu = 0.25$, where it is possible to observe the finer wake mesh in the vicinity of the trailing edge, as well as the regularity of the distortion of the surface. The wake consists of 144 panels in azimuth, integrated using 216 time steps per revolution. Each blade is discretized using 16 panels in radial direction and 10 panels in chord. A mesh of this quality can be considered accurate for analysis in forward flight.

2.3 Fluid-Structure Interaction

The coupling of the aerodynamic BEM solver with the free general-purpose multibody solver MBDyn represents a key aspect of this study. A general approach has been chosen, in order to exploit the general communication and field mapping capabilities provided by the MSD solver.

In the current implementation, the structural and the aerodynamic solver are run as separate processes, and communicate using standard UNIX sockets (either local or inet). The MSD

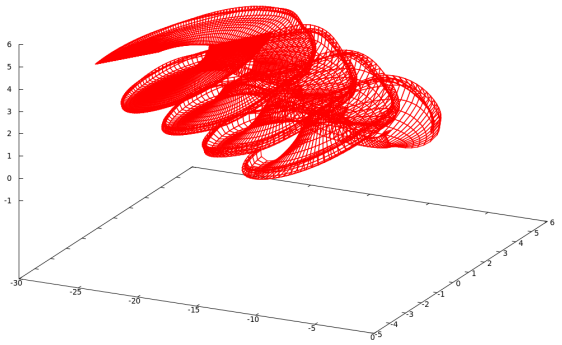

Figure 2: Distorted wake shape from free-wake analysis of a two-blade helicopter rotor in forward flight.

solver sends information about the kinematics of the structural model to the aerodynamic solver, and receives the aerodynamic loads in response. The two domains are mapped using a linear projection that extracts generalized information from the beam-based FEM modeling of the rotor and projects it on the Ritz shapes used by the BEM solver to model the deformation of the fluid-body interface, including rigid-body motion related, for example, to the rigid flap, lag and pitch blade motion of an articulated rotor. The generalized loads provided by the BEM solver are projected back on the FEM nodes of the MSD model by the projector conjugated to the previous one. This guarantees that both models experience the same amount of work done by the interface forces for the interface displacements [23].

The absolute motion of an arbitrary structural node i of the MSD model is described by its orientation $\mathbf{R}_i$ and location $\mathbf{x}_i$. The configuration of node i, expressed in the relative reference frame represented by the orientation and the location of another node, r (the hub node, in the present analysis), is

$$\tilde{\mathbf{R}}_i = \mathbf{R}_r^T \mathbf{R}_i \tag{5a}$$

$$\tilde{\mathbf{x}}_i = \mathbf{R}_r^T \left(\mathbf{x}_i - \mathbf{x}_r\right), \tag{5b}$$

where the tilde $\tilde{(\cdot)}$ indicates quantities in the relative reference frame. The differentiation of arbitrary rotations is defined in terms of the derivative of the orientation matrix. For example, the angular velocity ω_i is defined as $\omega = \mathrm{ax}(\dot{\mathbf{R}}\mathbf{R}^T)$, where $\mathrm{ax}(\cdot)$ is the inverse of the cross-product operator $(\cdot)\times$. Similarly, the virtual rotation is $\theta_\delta = \mathrm{ax}(\delta\mathbf{R}\mathbf{R}^T)$. The

linear and angular velocity of node i are

$$\tilde{\omega}_i = \mathbf{R}_r^T (\omega_i - \omega_r) \tag{6a}$$

$$\dot{\tilde{\mathbf{x}}} = \mathbf{R}_r^T (\dot{\mathbf{x}}_i - \dot{\mathbf{x}}_r) + \tilde{\mathbf{x}}_i \times \mathbf{R}_r^T \omega_r. \tag{6b}$$

The relative motion is

$$\tilde{\mathbf{R}}_i \cong \tilde{\mathbf{R}}_i (\mathbf{H}_\mathbf{R} \mathbf{q}) \tag{7a}$$

$$\tilde{\mathbf{x}}_i \cong \tilde{\mathbf{x}}_{0i} + \mathbf{H}_\mathbf{x} \mathbf{q} \tag{7b}$$

when it is small enough to be approximated by the linear combination of a set of shape functions $\mathbf{H}_\mathbf{x}$, $\mathbf{H}_\mathbf{R}$ weighted by the multipliers $\mathbf{q}$.

As soon as $\tilde{\theta}_i \cong \mathbf{H}_\mathbf{R} \mathbf{q}$ is small enough, the first-order approximation

$$\tilde{\mathbf{R}}_i \cong \mathbf{I} + (\mathbf{H}_\mathbf{R} \mathbf{q}) \times \tag{8}$$

can be used for the relative orientation.

After defining $\tilde{\theta}_\delta$ and $\delta\tilde{\mathbf{x}}$ as the collection of the virtual rotations and displacements of all nodes, and $\delta\mathbf{q}$ as the virtual perturbations of the modal variables, the mapping

$$\begin{bmatrix} \mathbf{H}_\mathbf{x} \\ \mathbf{H}_\mathbf{R} \end{bmatrix} \delta\mathbf{q} = \begin{Bmatrix} \delta\tilde{\mathbf{x}} \\ \tilde{\theta}_\delta \end{Bmatrix} \tag{9}$$

can be inverted, using the Moore-Penrose Generalized Inverse (MPGI), or pseudo-inverse, to yield the projection matrix $\mathbf{H}^+$ that projects the virtual relative motion of the nodes onto the space of the modal variables $\mathbf{q}$, namely

$$\mathbf{q} = \mathbf{H}^+ \begin{Bmatrix} \tilde{\mathbf{x}} - \tilde{\mathbf{x}}_0 \\ \tilde{\theta} \end{Bmatrix}. \tag{10}$$

The same transformation projects the velocities,

$$\dot{\mathbf{q}} = \mathbf{H}^+ \begin{Bmatrix} \dot{\tilde{\mathbf{x}}} \\ \tilde{\omega} \end{Bmatrix}. \tag{11}$$

According to the Virtual Work Principle (VWP), the virtual work of nodal forces and moments, $\tilde{\mathbf{f}}$ and $\tilde{\mathbf{m}}$, is equal to that of the generalized forces $\mathbf{p}$, conjugated to the generalized coordinates $\mathbf{q}$, namely

$$\tilde{\theta}_\delta^T \tilde{\mathbf{m}} + \delta\tilde{\mathbf{x}}^T \tilde{\mathbf{f}} = \delta\mathbf{q}^T \mathbf{p}. \tag{12}$$

Considering the virtual perturbation of the mapping of Eq. (10), the nodal forces are

$$\begin{Bmatrix} \tilde{\mathbf{f}} \\ \tilde{\mathbf{m}} \end{Bmatrix} = \left(\mathbf{H}^+\right)^T \mathbf{p}, \tag{13}$$

whose virtual work is equivalent to that of the generalized forces. In the absolute frame, the force and moment related to the i-th node result in

$$\mathbf{f}_i = \mathbf{R}_r \tilde{\mathbf{f}}_i \qquad i \neq r \tag{14a}$$

$$\mathbf{f}_i = -\mathbf{R}_r \sum_j \tilde{\mathbf{f}}_j \qquad i = r \tag{14b}$$

$$\mathbf{m}_i = \mathbf{R}_r \tilde{\mathbf{m}}_i \qquad i \neq r \tag{14c}$$

$$\mathbf{m}_i = -\mathbf{R}_r \sum_j \left(\tilde{\mathbf{m}}_j + \tilde{\mathbf{x}}_j \times \tilde{\mathbf{f}}_j\right) \qquad i = r. \tag{14d}$$

The contributions of force and moment applied to the generic nodes to the force and moment in node r need to be subtracted, according to Eqs. (14b) and (14d), from the corresponding rigid-body rotor force and moment computed by the BEM solver.

The BEM solver models the deformation of the blade as the linear combination of lag, flap and torsion modes, including rigid modes (i.e. articulated rotor lag and flap, and rigid pitch) if needed. Further details are given in [10, 12].

The coupling procedure, from the point of view of the MSD solver, is:

1. transform the configuration of participating structural nodes in the reference frame of node r according to Eqs. (5) and (6);
2. compute the modal variables $\mathbf{q}$ and their derivatives according to the mapping of Eqs. (10) and (11);
3. pass the mapped motion and the motion of node r to the BEM solver;
4. receive the generalized forces and the rigid-body forces and moments from the BEM solver;
5. transform the generalized forces in nodal forces and moments according to Eq. (13);
6. transform the nodal forces from the reference frame of node r into the absolute reference frame according to Eqs. (14).

The two solvers are tightly coupled; in fact, they can communicate at each iteration, thus converging cooperatively within each time step. In most analyses, however, the wake geometry can be considered frozen within the time step. In those cases, the coupling, although formally tight, actually consists in a single exchange, which corresponds to the kinematics predicted, for that time step, by the numerical integration algorithm used by the MBS solver. The MSD solver subsequently

iterates as required to converge with the resulting aerodynamic loads.

This approach allows to exploit the points of strength of the BEM and of the MSD solver in the analysis of this intrinsically multidisciplinary problem. In fact, as reported in earlier analyses [8], the appearance of adverse couplings is related to simultaneously considering

1. pilot's biodynamic feedthrough,
2. rigid-body motion of the rotorcraft,
3. compliance of the blades and
4. compliance of the airframe,

all interacting through the aerodynamics of the rotor.

2.4 Interaction with the Pilot

The distinguishing aspect of the present work consists in considering the interaction between the aeroelasticity of the helicopter and the pilot biodynamic feedthrough. A complete analysis needs to consider:

- how airframe vibrations are transmitted to the pilot's body;
- how the vibration of the pilot is transmitted to the control inceptors;
- how the motion of the control inceptors is transmitted to the rotor actuators;
- how the commanded motion of the actuators is transformed in rotor controls.

In modern rotorcraft, with partial or full authority Automatic Flight Control System (AFCS), the motion of the control inceptors is filtered and combined with other inputs, generated by the AFCS, before being fed to the control actuators. However, in this work the AFCS is not considered.

Some of the above mentioned aspects have been already addressed, at least preliminarily, in previous works [8, 10], and thus are only briefly described in the following.

The pilot models are coupled with the system within the MSD solver. So-called General-purpose elements (GENEL) allow to model arbitrary system dynamics. The passive pilot is modeled as a State Space (SS) representation of a Multi-Input Multi-Output (MIMO) system[1]. It receives in input the absolute acceleration of the seat, and outputs the motion of the control inceptors, namely the collective bar and the cyclic stick. Since this work focuses on the collective bounce problem, only the collective control is considered.

[1]Multiple-SISO (MSISO) would be a more appropriate name, since in currently available models all axes are independent.

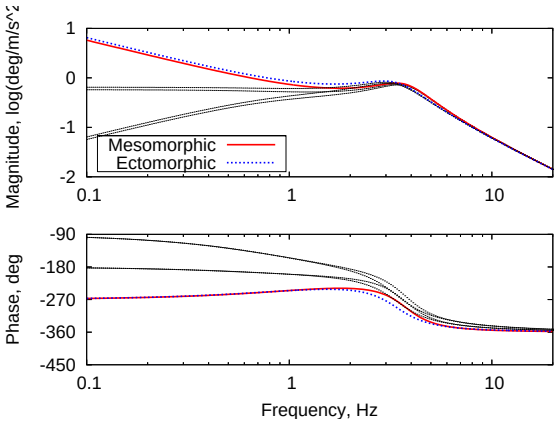

Figure 3: Pilot transfer functions from [2], modified to yield the relative rotation.

The transfer functions $H_{\text{abs}}(s)$ proposed by Mayo [2] describe the absolute acceleration of the collective handle with respect to the absolute acceleration of the seat, $a(s)$, for the so-called 'ectomorphic' (smaller size) and the 'mesomorphic' (larger size) pilots, They need to be transformed into the (relative) rotation of the collective bar as a function of the vertical acceleration of the seat.

$$H_{\text{abs, meso}} = \frac{4.02s + 555.4}{s^2 + 13.31s + 555.4} \tag{15a}$$

$$H_{\text{abs, ecto}} = \frac{5.19s + 452.3}{s^2 + 13.70s + 452.3}. \tag{15b}$$

The relative acceleration, namely the acceleration of the pilot's hand with respect to the acceleration of the cockpit is $H_{\text{rel}}(s) = H_{\text{abs}}(s) - 1$. The rotation of the bar is obtained by dividing the relative acceleration by the distance L between the collective bar hinge and the point where the pilot grabs the stick, and by integrating twice,

$$\Delta\theta(s) = \frac{1}{s^2}\frac{1}{L}\left(H_{\text{abs}}(s) - 1\right)a(s). \tag{16}$$

When this transformation is applied to Eqs. (15), the transfer functions of Fig. 3 result. The presence of two integrators $1/s^2$ in Eq. (16) yields a drifting behavior when $s \to 0$. This is not physical, as it would imply, for example, that the collective reduces indefinitely because of gravity. What this experimental transfer function is missing is the fact that the pilot's active behavior will compensate any

low-frequency change of collective inceptor position as soon as it is adequately detected. To account for this, the functions are high-pass filtered by turning the integrator poles $1/s^2$ into stable real poles α_1, α_2 close to zero ($\alpha_i < 0$), namely

$$\Delta\theta(s) = \frac{1}{(s-\alpha_1)(s-\alpha_2)} \frac{1}{L} \left(H_{\text{abs}}(s) - 1\right) a(s). \quad (17)$$

The dashed lines in Fig. 3 illustrate this correction. They correspond to turning either one or both the integrators into one or two poles at 1 Hz. The 'active' pilot behavior, in previous analyses, was delegated to a simple PD regulator with very low gains, in order to minimize its interaction with the dynamics of the system in the frequency range of interest, while loosely flying the helicopter in the desired flight condition [8, 10, 12]. Alternatively, exploiting McRuer's crossover model [24, 25], the active pilot model can be obtained by considering that the open-loop behavior of the aircraft and the pilot can be represented as

$$H_{\text{OL}}(s) = G_c \, H_{\text{pilot}}(s) \, H_{\text{aircraft}}(s) = -\frac{\omega_c}{s} \mathrm{e}^{-\tau_e s}, \quad (18)$$

i.e. the combination of an integrator and a human operator time delay τ_e with a given crossover frequency ω_c that usually show some task dependence. The term G_c represents the gearing factor between the control inceptor and the actual motion of the related control surface. Considering for $H_{\text{aircraft}}(s)$ a low-order approximation of the rotorcraft dynamics about the axis under consideration, the active pilot model can be obtained as

$$H_{\text{pilot}}(s) = -H^{-1}_{\text{aircraft}}(s) \frac{\omega_c}{s G_c} \mathrm{e}^{-\tau_e s}. \quad (19)$$

In the case of the vertical bouncing, a minimal rotorcraft model that describes the vertical position z as a function of the collective control θ is $M\ddot{z} = Z(\dot{z}, \theta)$, where M is the mass of the helicopter, while Z is the thrust of the rotor. Its linearization, in the Laplace domain, is

$$H_{\text{aircraft}} = H_{z\theta} = \frac{Z_{/\theta}}{s\left(sM - Z_{/\dot{z}}\right)}, \quad (20)$$

with $Z_{/\theta} > 0$, $Z_{/\dot{z}} < 0$, thus the model of the aircraft is asymptotically stable and can be inverted. In this case, G_c is the gearing factor between the collective stick rotation and the collective pitch of the blades. The resulting pilot model is

$$H_{\text{pilot}}(s) = \frac{\omega_c Z_{/\dot{z}}}{G_c Z_{/\theta}} \left(1 - s\frac{M}{Z_{/\dot{z}}}\right) \mathrm{e}^{-\tau_e s}. \quad (21)$$

Table 1: Crossover pilot model data.

M	2200.	kg
$Z_{/\theta}$	4000.	N/deg
$Z_{/\dot{z}}$	−1400.	N·s/m
ω_c	3.10	radian/s
τ_e	0.33	s

An estimate of the values appropriate for a helicopter of the class of the Bo-105 for the vertical positioning task are reported in Table 1, where ω_c and τ_e may show some limited dependence on the frequency ω_i that characterizes the task [24]. To implement this model in a time marching simulation, the delay can be realized in rational polynomial form using a Padé approximation of the first,

$$\mathrm{e}^{-\tau_e s} \cong \frac{1 - \frac{1}{2}\tau_e s}{1 + \frac{1}{2}\tau_e s}, \quad (22)$$

or of the second order,

$$\mathrm{e}^{-\tau_e s} \cong \frac{1 - \frac{1}{2}\tau_e s + \frac{1}{12}(\tau_e s)^2}{1 + \frac{1}{2}\tau_e s + \frac{1}{12}(\tau_e s)^2}, \quad (23)$$

although a higher-order one might be more appropriate.

Figure 4 shows the aircraft and active pilot transfer functions that produce the desired crossover at ω_c = 3.10 radian/s. The figure highlights the error in phase provided by Padé's first and second order approximations; the second order one is negligible up to 1 Hz. The pilot's transfer function of Eq. (21) is not realizable, as the number of zeros exceeds that of poles. In practice, this means that high-frequency input is excessively amplified, something counter-intuitive in a pilot model, since one expects the pilot to be unable to act on the controls beyond a well limited bandwidth. In order to prevent this spill-over, the input to the active pilot is low-pass filtered by a second-order Butterworth filter

$$H_{\text{filter}}(s) = \frac{1}{1 + \sqrt{2}\frac{s}{\omega_b} + \left(\frac{s}{\omega_b}\right)^2} \quad (24)$$

with cut frequency $\omega_b = 3\omega_c$.

More sophisticated models, like the human Optimal Control Model (OCM), show a similar behavior [26]. Both approaches yield a behavior that is

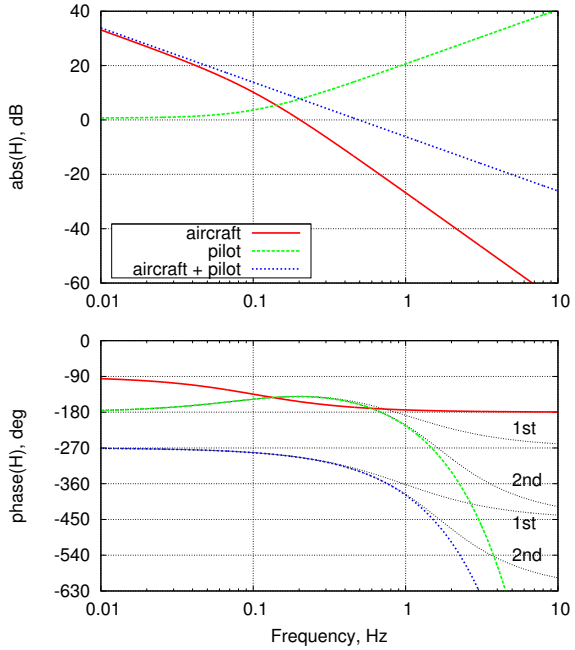

Figure 4: Active pilot based on crossover model.

roughly analogous to Hess' Structural Pilot Model (SPM) [27], with emphasis on the biomechanical behavior.

In this work, the main parameter affecting the RPC is the gain G that scales the action of the pilot on the collective stick with respect to the pitch of the blades. This parameter can be thought of as the sensitivity of the blade collective pitch control to the motion of the inceptor. In conventional helicopter controls, this parameter is usually defined as a linear mapping between the collective pitch range (for example, 0 to 20 deg) and the ergonomically acceptable excursion of a conventional collective stick. An increase in G corresponds to reducing the excursion of the control inceptor for a given range of collective pitch.

2.5 Actuation System

The outputs are transformed into swashplate commands after additional filtering, intended to represent the dynamics of the actuation system. For example, the dynamics of the hydraulic actuators that command the swashplate motion are typically expressed using first- or second-order transfer functions, e.g.

$$y = \frac{1}{1+\tau s} u \tag{25}$$

Table 2: Airframe Modes

Mode	Freq., Hz
#1 Tail boom vertical bending	6.0
#2 Tail boom lateral bending	8.0
#3 Fuselage vertical bending	11.5
#4 Tail boom torsion	12.5

or

$$y = \frac{1}{1+2\zeta s/\omega_0 + s^2/\omega_0^2} u, \tag{26}$$

where $u = G\Delta\theta$ is the actuator elongation commanded by the pilot, while y is the actual elongation. The MSD model of the control system kinematics transforms the actuator elongation into the appropriate blade pitch.

In principle, within the MSD approach the impedance of the actuators can also be considered, and nonlinear effects like friction, saturation, freeplay, backlash can be added. These effects, for example, may characterize Cat. II PIO [1]. However, they are beyond the scope of this work, as they typically impact RPC related to 'intentional' pilot inputs.

3 Results

3.1 Model Description

The model is representative of a lightweight helicopter with hingeless rotor design, loosely inspired by the Bo-105. The structural dynamics of the airframe and the aerodynamics and structural dynamics of the main rotor are modeled. The tail rotor dynamics and aerodynamics are neglected, since the airframe is constrained to only allow free vertical motion. The dynamics of the control system are accounted for using a first-order transfer function. Only the pilot models proposed by Mayo [2] have been considered.

The airframe is described by 4 NVM, reported in Table 2 (frequencies are approximate). A modal survey, correlated with numerical analysis, was provided in [28]. The first mode involves significant bending of the airframe about the pitch axis, and significant out of phase relative vertical motion between the main rotor attachment and the cabin floor, thus possibly introducing non-negligible interaction between the vertical oscillation of the rotorcraft and that of the pilot's and co-pilot's seats. However, all mode shapes show some participation of those points, as discussed later.

When analyzed by the BEM solver, the main rotor has been modeled using three elastic modes for flap and lag, and one rigid and two elastic modes for torsion. The rigid torsion mode represents the actual rotation of the blade about the pitch bearing, thus accounting for both the imposed pitch and that resulting from the compliance of the control system. Each blade is dealt with independently, so a total of $(3+3+3)\cdot 4 = 36$ modes are considered, while the finite element model of the rotor consists of $11 \cdot 4 = 44$ structural nodes. Since only section-wise displacement and torsion participate in the mapping, a total of 132 out of 264 nodal degrees of freedom are involved. Formally, the projection matrix $\mathbf{H}^+$ of Eq. (10) is 36 by 264; however, owing to its significant sparsity, it contains only 372 non-zeros, for a 3.9% fill-in. Since the matrix is only used for matrix-vector multiplications, either direct or transpose, its sparsity is heavily exploited, thus minimizing the computational effort related to the mapping.

The free wake is modeled using 160 panels in azimuth. The structural dynamics are integrated using 100 time steps per revolution. The blade is meshed using 14 panels in the radial and 10 in the chordwise direction. Aeroservoelastic analysis with free wake are correlated with corresponding analysis performed using Pitt-Peters' dynamic inflow model [29] coupled to blade element aerodynamics, which are available within the multibody dynamics analysis.

Since a non-trivial detailed nonlinear aeroservoelastic model is being analyzed, a special procedure is needed in order to initialize the analysis as appropriate. Instead of resorting to a specialized steady solution, trimmed initial conditions are obtained by solving a modified transient. The structural dynamics model is initially clamped to the ground at the CM of the airframe. The main rotor is rotating at full rpm (Ω_{main} = 44.4 radian/s). The collective control is defined as

$$\theta_0 = \theta_{0\ \text{nominal}} + \Delta\theta_{0\ \text{autopilot}} + \Delta\theta_{0\ \text{pilot}} + \Delta\theta_{0\ \text{excitation}} \tag{27}$$

where $\Delta\theta_{0\ \text{pilot}}$ is computed according to Eq. (17), while $\Delta\theta_{0\ \text{autopilot}}$ is either computed by a dedicated Proportional-Derivative (PD) controller or by a crossover-based active pilot model according to Eq. (21) that makes the rotorcraft follow the prescribed trajectory (constant height in the present case); $\Delta\theta_{0\ \text{excitation}}$ introduces an excitation in the system.

3.2 Aeroelastic Analysis in Hover

Figure 5 shows the main rotor thrust (top) and the vertical acceleration of the center of mass (CM) of the aircraft (bottom) after the initial trim phase (which takes place from 0 to 20 rev) and during a subsequent phase in which a $(1-\cos)$ excitation is introduced at about 35 revolutions according to

$$\Delta\theta_{0\ \text{excitation}} = A\,(1-\cos(\omega t)) \tag{28}$$

with A = 1 deg and ω = 2·π·5 radian/s for 5 s $< t <$ 5.2 s; $\Delta\theta_{0\ \text{pilot}}$ is zero.

As one would expect, there is a direct correspondence between the rotor thrust and the vertical acceleration of the airframe. The free wake analysis seems to yield a fair correspondence with dynamic inflow in terms of peak to peak amplitude, with a slightly different frequency of the vertical bounce mode, i.e. the coupled rotor collective cone-airframe mode. The free wake thrust and acceleration are not as smooth as those of the blade element analysis owing to the intrinsically transient nature of the free wake analysis.

Coupled BEM/MSD analyses of RPC in hover are not specifically addressed because they were discussed in some detail in [10], in an early implementation of the coupling. Focus is rather placed on analysis in forward flight, which is the subject of the subsequent section. Hover analyses are considered in subsequent sections to highlight the sensitivity of the collective bounce RPC to other parameters of the analysis.

3.3 Aeroelastic Analysis in Forward Flight

Figure 6 shows the main rotor thrust (top) and the acceleration of the center of mass of the airframe (bottom) after the initial trim phase, and during an excitation phase where a collective "doublet" is applied, consisting of two $(1-\cos)$ functions of amplitude 0.5 deg of opposite sign, the second one phased half period after the first one. The 4/rev oscillation in the thrust is clearly visible in the free wake analysis, while it is somehow partially smoothed out by the dynamic inflow. However, the transient response of the two analyses is quite similar.

Figure 7 shows the acceleration of the center of mass of the airframe (top) and the pilot's control (bottom) at different gain levels from blade element analysis. The solution is unstable for a gain G = 1.2. The diverging oscillation occurs at about 0.55/rev, which corresponds to 3.92 Hz, slightly above the frequency of the pilot's pole. An identifi-

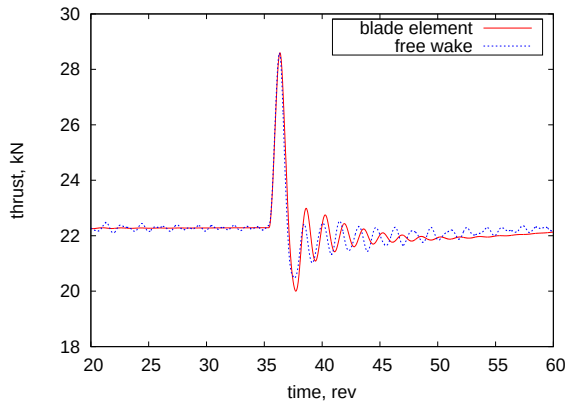

(a) Thrust.

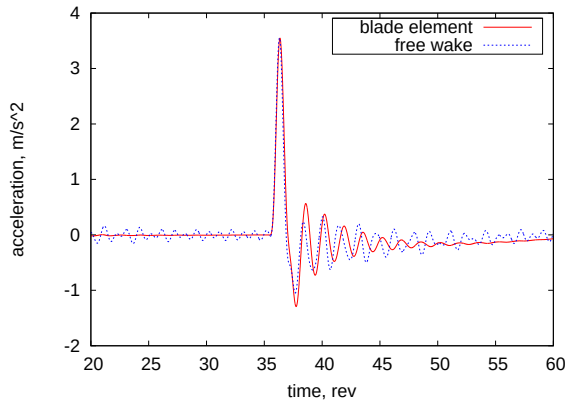

(b) Vertical acceleration.

Figure 5: Thrust and vertical acceleration of the airframe CM without passive pilot participation.

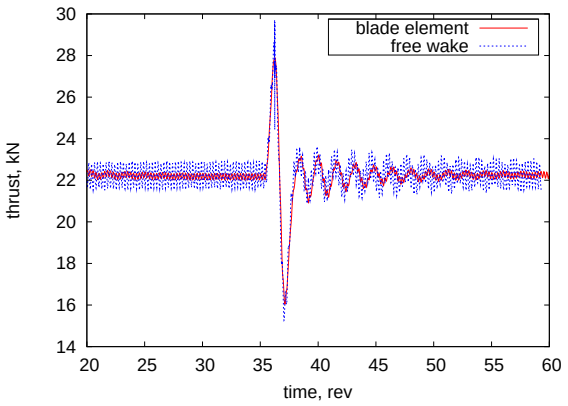

(a) Thrust.

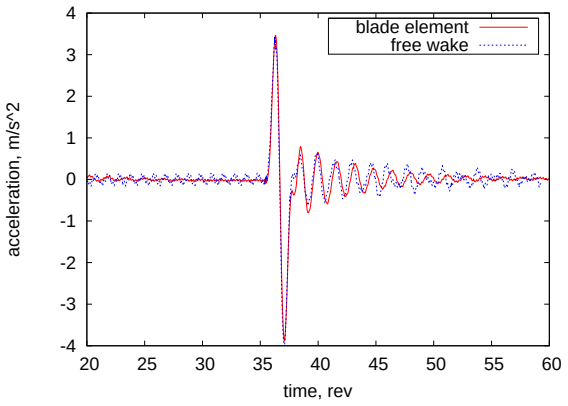

(b) Vertical acceleration.

Figure 6: Thrust and vertical acceleration of the airframe CM without passive pilot participation.

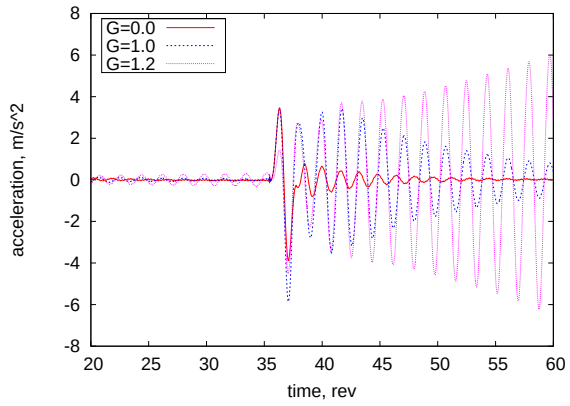

(a) Vertical acceleration.

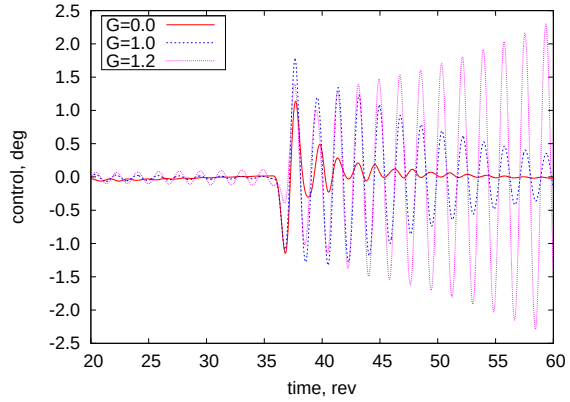

(b) Pilot control, $\Delta\theta_{0\ \text{pilot}}$.

Figure 7: Vertical acceleration of the airframe CM and pilot control for different values of pilot gain, G.

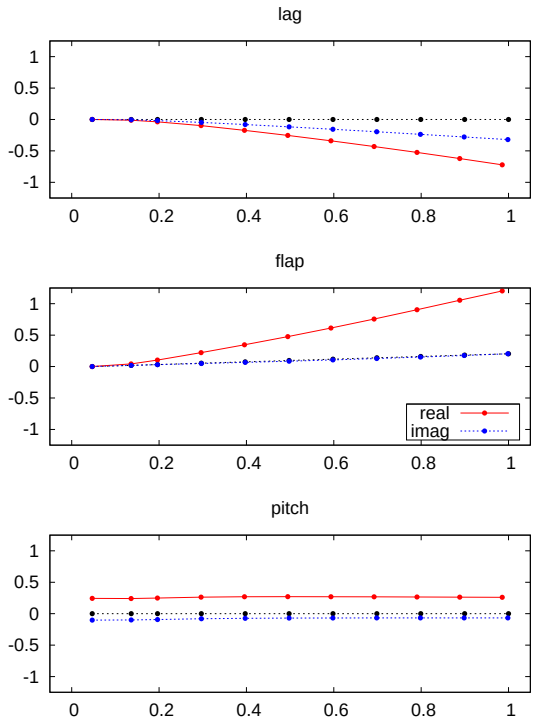

Figure 8: Unstable mode shape in forward flight for G = 1.2.

cation of the time response from time series after reducing the motion by means of a Proper Orthogonal Decomposition (POD), as illustrated in [30], yields the blade mode shape shown in Fig. 8. The mode shape clearly shows a predominance of the first flap mode with a significant participation of the first lead-lag mode and of essentially rigid pitch, introduced by the pilot by means of the collective control. The blade flapping is slightly preceded by pitching, so it appears to be a consequence of the increased lift due to the pitching introduced by the pilot. The lag motion follows, essentially because the increase in pitch results in increased drag, and because the flap principal axis tilts backwards with pitching. The same oscillation, for G = 0, occurs at a slightly higher frequency, about 4.05 Hz.

Figures 9 and 10 compare the acceleration of the center of mass of the airframe (top) ad the pilot's control (bottom) at G = 1.1 and 1.2 for the blade element and the free wake analyses. In the first case (G = 1.1), very similar trends, in terms of response to the excitation and stability of the perturbed solution, are observed. In the second one (G = 1.2), whereas the blade element analysis shows a clean diverging oscillation shortly after the excitation ends, the free wake show a sort of an erratic behavior, which can probably be interpreted as the result of the initially unstable behavior that strongly interacts with the wake.

In both cases, the amplitude and the frequency of the excitation have been further divided by two, to cure convergence issues in the analysis coupled with free wake. The nearly sustained oscillations that appear before the excitation are related to the interaction with the pilot, which does not allow the analysis to reach a steady condition after starting from perturbed initial conditions, since the rotorcraft-pilot mode is only marginally stable, or unstable.

3.4 Influence of Active Pilot

The influence of the active pilot model on the stability of the problem has been considered by replacing the intentionally very low bandwidth autopilot with the crossover-based pilot model of Eq. (21). Stability results are not significantly af-

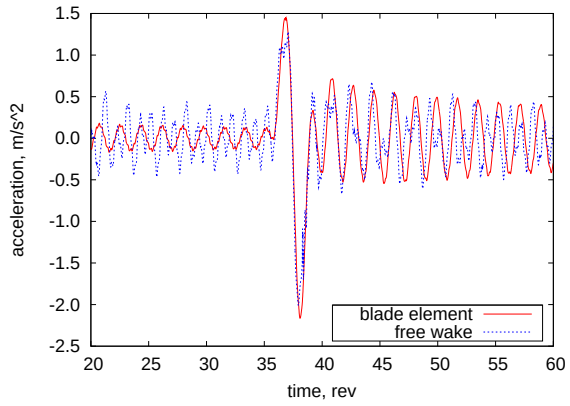

(a) Vertical acceleration.

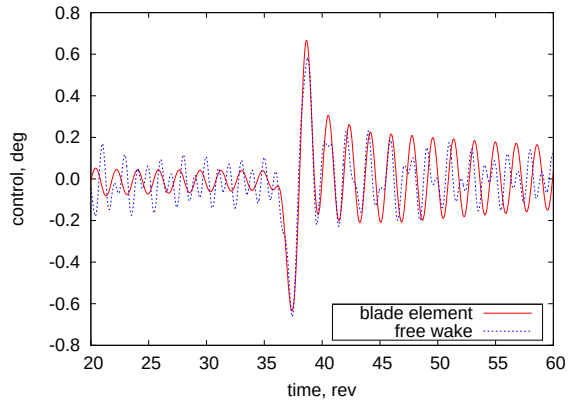

(b) Pilot control, $\Delta\theta_{0\ \text{pilot}}$.

Figure 9: Vertical acceleration of the airframe CM and pilot control for G = 1.1.

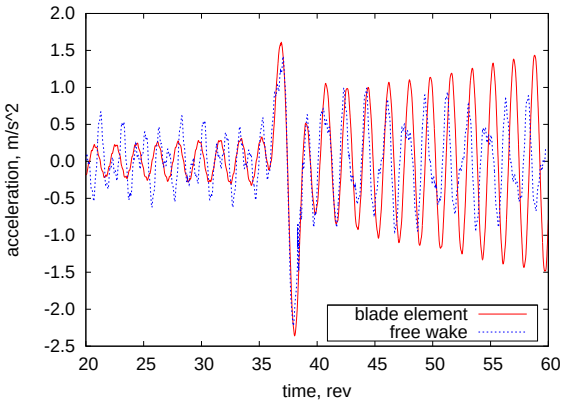

(a) Vertical acceleration.

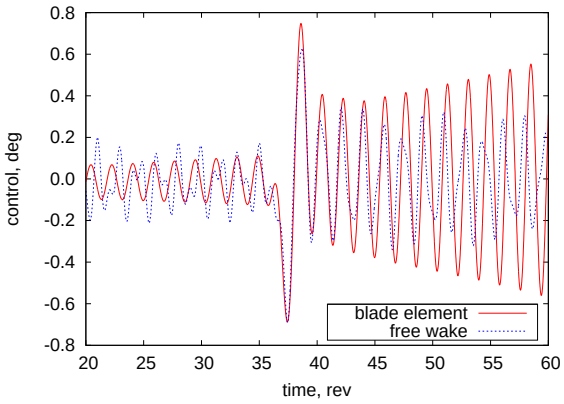

(b) Pilot control, $\Delta\theta_{0\ \text{pilot}}$.

Figure 10: Vertical acceleration of the airframe CM and pilot control for G = 1.2.

fected, as soon as adequate low-pass filtering is applied to the input of the active pilot function, to prevent its intervention in response to oscillations caused by the passive pilot model. However, the active pilot model shows a radically different behavior with respect to the admittedly oversimplified autopilot used in previous analyses. For example, consider the limit case of prescribing a desired step change of vertical position, something that resembles the transition phase of the vertical maneuver described in ADS33 [31].

Figure 11(a) illustrates the prescribed and the actual vertical displacement without (G = 0) and with the passive pilot model in marginal stability conditions (G = 0.85). The crossover-based active pilot model responds to a step input with a delay that is consistent with τ_e (about 0.3 s). When no passive pilot model is considered the response is very prompt, with appreciable overshooting. When the passive pilot model is considered the response is appreciably slower. The presence of minimal oscillations, associated with vertical bouncing, can be barely noticed. However, Fig. 11(b) clearly shows how the relatively sharp response of the active pilot triggers the vertical bounce oscillation. In this sense, the main effect of considering a more realistic, although simple active pilot model, is the triggering of aeroelastic RPC events associated to performing relatively realistic tasks. Figure 11(c) shows the collective angle in response to the step vertical position input. The response of the passive pilot model (the curve labeled 'passive') clearly shows a non-negligible low frequency content, interfering with the active pilot model response (the curve labeled 'active'). This explains the much slower response of Fig. 11(a), as soon as the oscillation develops, when G = 0.85. This effect is purely numerical; it is dictated by the fact that the passive pilot model has been arbitrarily corrected by a high-pass filter at 0.1 Hz; a higher value, say 0.5 Hz, would probably reduce the amount of overlapping between the two models.

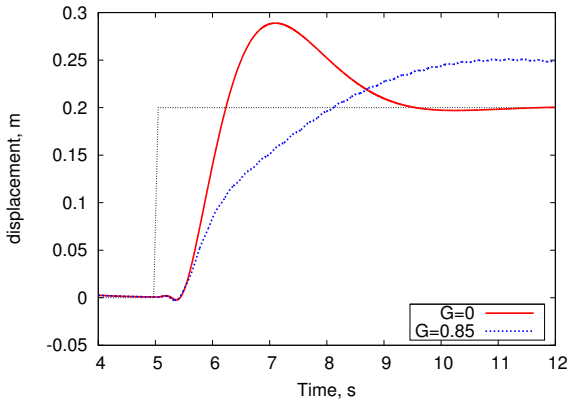

(a) Vertical displacement

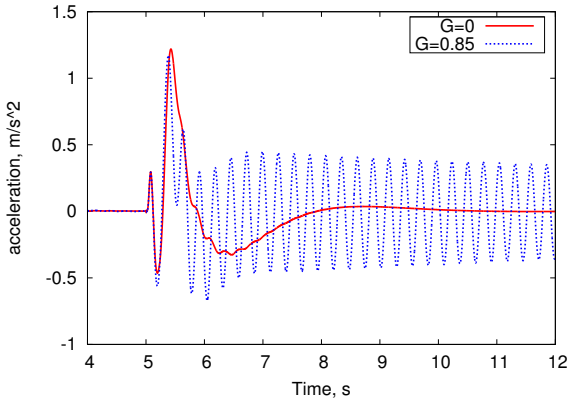

(b) Vertical acceleration

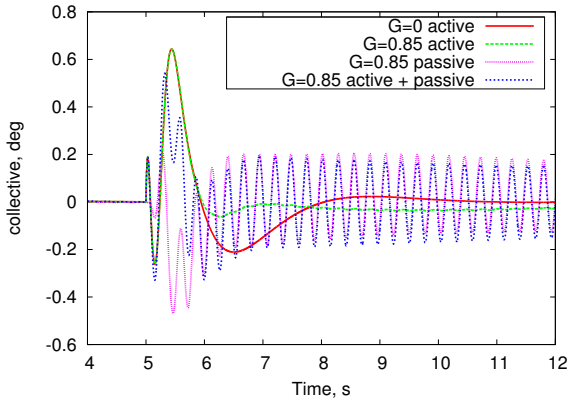

(c) Collective angle

Figure 11: Response to step input.

Table 3: Dependence of pilot mode damping on airframe modes in hover.

Case	damping factor, %
No Pilot	
No modes	8.3
Modes #1 + #2 + #3 + #4	8.5
Pilot, G = 0.85	
No modes	3.2
Mode #1 only	1.7
Mode #2 only	2.1
Mode #3 only	2.5
Mode #4 only	3.4
Modes #1 + #2	1.0
Modes #1 + #3	1.7
Modes #2 + #3	1.7
Modes #1 + #2 + #3	0.7
Modes #1 + #2 + #3 + #4	0.7

3.5 Influence of Airframe Dynamics

Table 3 shows how the type and number of airframe modes considered in the analysis may impact the stability of the problem. When the pilot is disconnected (G = 0), the problem shows a pair of poles at about 4.5 Hz associated to the rotor collective flap. Regardless of the number and type of airframe modes considered, this pole shows a damping of about 8.5%. When the pilot is in the loop (sitting in the "pilot" seat, using Mayo's mesomorphic transfer function, with high-pass filtering at 0.1 Hz) and all four airframe modes are considered, a gain G = 0.85 provides marginal stability (0.7%). In this case, when no airframe modes are considered, the damping jumps to 3.2%. When each airframe mode is independently activated, the damping never reduces to less than 1.7%; the higher the number of the mode that is activated, the higher the damping. Mode #4 seems to have no impact on stability, since the damping factor is the same as in the case of no active modes. However, modes #1 to #3 seem to have some role, since when only a subset of them is active the damping is higher than with the nominal case. This seems to indicate that: 1) the model considered in this analysis is at convergence; 2) airframe flexibility plays an important role in the stability of the system, further justifying the "aeroelastic" characteristic of the problem; 3) only modes #1 and #2 may have a dynamic role in the instability, while mode #3 should only play a static role since its frequency is clearly separated from the one that becomes unstable.

3.6 Influence of Blade Compliance

The compliance of the rotor plays an important role in the aeroelastic RPC mechanism. This aspect has not been investigated in detail, as in most analyses a nominal aeroelastic model of the rotor has been considered. However, after noticing that despite the nearly rigid pitch motion in the unstable mode shape shown in Figure 8 some torsion of the blade occurs, the blade has been made torsionally rigid by increasing the torsional stiff GJ by a factor 10^4. This resulted in a reduction of the trim collective by about 1.2 deg.

Figures 12 and 13 compare the vertical acceleration of the rotorcraft CM in the nominal and torsionally rigid case with G respectively equal to 0 and 0.85. Figure 8 clearly indicates that the phenomenon is dominated by rigid blade pitch; however, elastic torsion of the blade significantly affects the stability of the problem, basically eliminating the instability. The instability occurs when the gain is increased to G = 1.08, more than 25% higher than the value G = 0.85 for the nominal stiffness. It is worth stressing that in this case the torsion of the blade is essentially static, since the lowest torsional mode is at about 28 Hz, thus nearly one decade above the unstable mode.

3.7 Computational Cost

The analyses presented in this work have been performed over a long period of time and on different machines of comparable performances. Typical simulations required to perform 70 main rotor revolutions and 7000 time steps, for about 10 s of simulated time. The blade element analysis

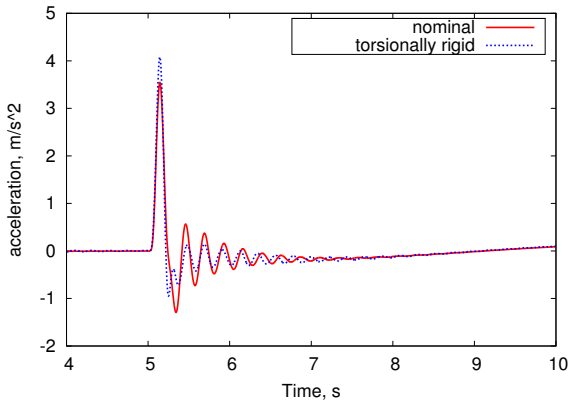

Figure 12: CM vertical acceleration with torsionally stiff blade: G = 0 (no pilot).

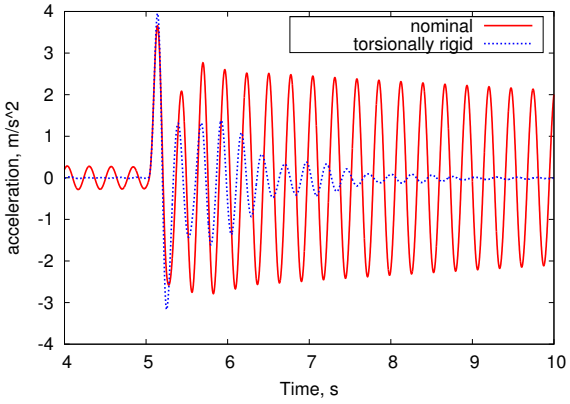

Figure 13: CM vertical acceleration with torsionally stiff blade: G = 0.85.

is very efficient: aeroelastic models consisting of about 700 equations run in 3 to 4 times realtime, since 10 s of simulated time are executed in 30 to 40 s, depending on analysis complexity and time step used (100 to 120 steps per rotor revolution). The free wake analysis has a significant computational cost, compared to the structural dynamics and blade element case. The analyses coupled with free wake have been run on an Intel(R) Core i7 CPU 930, 2.80 GHz. The coupled analysis with free wake runs on four cores in about 3 hours.

4 Conclusions

The paper discusses a numerical investigation of aeroelastic Rotorcraft-Pilot Coupling problems, performed with a comprehensive rotorcraft aeroservoelastic analysis obtained by coupling a free wake analysis based on an original Boundary Element Method formulation and a general-purpose multibody dynamics software. Focus is placed on collective bounce, in hover and forward flight, highlighting several aspects related to the influence of the aerodynamic modelling, the influence of the structural dynamics of the airframe, and of the modeling of the pilot's behavior. Good correlation of results with blade element theory and dynamic inflow models has been shown.

Acknowledgments

The research leading to these results has received funding from the European Community's Seventh Framework Programme (FP7/2007-2013) under grant agreement N. 266073, and was partially supported by the Italian Ministry of University and Research under PRIN 20078TJFZE.

REFERENCES

[1] D. T. McRuer. *Aviation Safety and Pilot Control: Understanding and Preventing Unfavourable Pilot-Vehicle Interactions*. Washington DC: National Research Council, National Academy Press, 1997.

[2] John R. Mayo. The involuntary participation of a human pilot in a helicopter collective control loop. In *15th European Rotorcraft Forum*, pages 81.1–12, Amsterdam, The Netherlands, 12–15 September 1989.

[3] T. Parham, Jr. and David Popelka. V–22 pilot-in-the-loop aeroelastic stability analysis. In *47th Annual Forum of the American Helicopter Society*, Phoenix, Arizona (USA), May 6–8 1991.

[4] T. Parham, Jr. and Lawrence M. Corso. Aeroelastic and aeroservoelastic stability of the BA 609. In *25th European Rotorcraft Forum*, Rome, Italy, September 14–16 1999.

[5] R. Barry Walden. A retrospective survey of pilot-structural coupling instabilities in naval rotorcraft. In *63rd Annual Forum of the American Helicopter Society*, Virginia Beach, VA, May 1–3 2007.

[6] O. Dieterich, J. Götz, B. DangVu, H. Haverdings, P. Masarati, M. Pavel, M. Jump, and M. Gennaretti. Adverse rotorcraft-pilot coupling: Recent research activities in europe. In *34th European Rotorcraft Forum*, Liverpool, UK, September 16–19 2008.

[7] M. Jump, S. Hodge, B. DangVu, P. Masarati, G. Quaranta, M. Mattaboni, M. Pavel, and O. Dieterich. Adverse rotorcraft-pilot coupling: The construction of the test campaigns at the university of liverpool. In *34th European Rotorcraft Forum*, Liverpool, UK, September 16–19 2008.

[8] M. Gennaretti, J. Serafini, P. Masarati, G. Quaranta, and O. Dieterich. Aeroelastic and biodynamic modeling for stability analysis of rotorcraft-pilot coupling phenomena. In *34th European Rotorcraft Forum*, Liverpool, UK, September 16–19 2008.

[9] Jacopo Serafini, Massimo Gennaretti, and Giuliano Coppotelli. Influence of fuselage dynamics properties on rotorcraft-pilot coupling phenomena. In *XX AIDAA Congress*, Milano, Italy, June 29-July 3 2009.

[10] Pierangelo Masarati, Giuseppe Quaranta, Massimo Gennaretti, and Jacopo Serafini. Aeroservoelastic analysis of rotorcraft-pilot coupling: a parametric study. In *AHS 66th Annual Forum*, Phoenix, AZ, May 11–13 2010.

[11] J. Serafini, L. Greco, and M. Gennaretti. Prediction of rotorcraft-pilot coupling phenomena through reduced-order aerodynamic model. In *IFASD 2009*, Seattle, Washington, June 22–24 2009.

[12] J. Serafini, M. Gennaretti, P. Masarati, and G. Quaranta. Aeroservoelastic investigation of rotorcraft-pilot coupling (RPC) by coupled BEM/multibody analysis. In *IFASD 2011*, Paris, France, June 26–30 2011.

[13] J. Serafini, D. Muro, and M. Gennaretti. Pilot-in-the-loop influence on controlled tiltrotor stability and gust response. In *27th International Congress of the Aeronautical Sciences*, Nice, France, September 2010.

[14] P. Masarati, G. Quaranta, W. Basso, R. Bianco-Mengotti, and C. Monteggia. Preliminary in-flight biomechanic tests on the BA-609 fly-by-wire tiltrotor. In *21st SFTE EC Symposium*, Vergiate (VA), Italy, October 3–6 2010.

[15] M. Mattaboni, P. Masarati, V. Muscarello, G. Quaranta, and P. Mantegazza. Integrated flight dynamics and aeroservoelasticity modeling and control of tiltrotor aircraft using multibody simulation. In *IFASD 2011*, Paris, France, June 26–30 2011.

[16] Giuseppe Quaranta, Giampiero Bindolino, Pierangelo Masarati, and Paolo Mantegazza. Toward a computational framework for rotorcraft multi-physics analysis: Adding computational aerodynamics to multibody rotor models. In *30th European Rotorcraft Forum*, pages 18.1–14, Marseille, France, 14–16 September 2004.

[17] P. Masarati and J. Sitaraman. Tightly coupled CFD/multibody analysis of NREL unsteady aerodynamic experiment phase VI rotor. In *49th AIAA Aerospace Sciences Meeting*, Orlando, Florida, January 4–7 2011.

[18] Pierangelo Masarati, Marco Morandini, Giuseppe Quaranta, and Riccardo Vescovini. Multibody analysis of a micro-aerial vehicle flapping wing. In J. C. Samin and P. Fisette, editors, *Multibody Dynamics 2011*, Brussels, Belgium, July 4–7 2011.

[19] Gian Luca Ghiringhelli, Pierangelo Masarati, and Paolo Mantegazza. A multi-body implementation of finite volume beams. *AIAA Journal*, 38(1):131–138, January 2000. doi:10.2514/2.933.

[20] M. Karpel and D. Raveh. Fictitious mass element in structural dynamics. *AIAA Journal*, 34(3):607–613, 1996.

[21] M. Gennaretti and G. Bernardini. Novel boundary integral formulation for blade-vortex interaction aerodynamics of helicopter rotors. *AIAA Journal*, 45(6):1169–1176, 2007. doi:10.2514/1.18383.

[22] L. Morino. A general theory of compressible potential aerodynamics. CR 2464, NASA, 1974.

[23] Giuseppe Quaranta, Pierangelo Masarati, and Paolo Mantegazza. A conservative mesh-free approach for fluid structure interface problems. In *Coupled Problems 2005*, Santorini, Greece, May 24–27 2005.

[24] D. T. McRuer and H. R. Jex. A review of quasi-linear pilot models. *Human Factors in Electronics, IEEE Transactions on*, HFE-8(3):231–249, September 1967. doi:10.1109/THFE.1967.234304.

[25] Duane T. McRuer and Ezra S. Krendel. Mathematical models of human pilot behavior. Paper No. 146, Systems Technology, Inc., 13766 S. Hawthorne Boulevard Hawthorne, California 90250-7083, January 1974. AGARD AG 188.

[26] Peter M. Thompson and Duane T. McRuer. Comparison of the human optimal control and crossover models. In *AIAA Guidance, Navigation and Control Conference*, pages 1083–1090, Minneapolis, MN, USA, August 15–17 1988. AIAA-1988-4183.

[27] R. A. Hess. Theory for aircraft handling qualities based upon a structural pilot model. *Journal of Guidance, Control and Dynamics*, 12(6):792–797, 1989. doi:10.2514/3.20483.

[28] J. Stoppel and M. Degener. Investigations of helicopter structural dynamics and a comparison with ground vibration tests. *Journal of the American Helicopter Society*, 27(2):34–42, April 1982. doi:10.4050/JAHS.27.34.

[29] Dale M. Pitt and David A. Peters. Theoretical prediction of dynamic-inflow derivatives. *Vertica*, 5:21–34, 1981.

[30] Giuseppe Quaranta, Pierangelo Masarati, and Paolo Mantegazza. Assessing the local stability of periodic motions for large multibody nonlinear systems using POD. *Journal of Sound and Vibration*, 271(3–5):1015–1038, 2004. doi:10.1016/j.jsv.2003.03.004.

[31] Performance specification, handling qualifies requirements for military rotorcraft. ADS 33-E-PRF, US Army AMCOM, Redstone, Alabama, 2000.